Spark-plasma-sintering and finite element method: From the identification of the sintering parameters of a submicronic α-alumina powder to the development of complex shapes

Charles Manière, Lise Durand, Alicia Weibel, Claude Estournès

Spark-plasma-sintering and finite element method: From the identification of the sintering parameters of a submicronic α-alumina powder to the development of complex shapes

Charles Manière [a, c], Lise Durand [b], Alicia Weibel [a], Claude Estournès [a, c, *]

[a] Université de Toulouse, Institut Carnot CIRIMAT, UMR 5085 CNRS – Université Toulouse III Paul-Sabatier – INPT, 118 route de Narbonne, 31062 Toulouse Cedex 9, France
[b] CEMES, CNRS UPR 8011 and Université de Toulouse, 29 rue Jeanne Marvig, 31055 Toulouse, France
[c] CNRS, Institut Carnot CIRIMAT, 118 route de Narbonne, 31602 Toulouse Cedex 9, France

A B S T R A C T

In the present paper, we studied the sintering of a submicronic α-alumina powder and modeled its behavior using Olevsky's model. We further introduced a method for the identification of the creep parameters based on SPS experiments that greatly simplify parameter determination. Subsequently, we used the set of parameters obtained to study the densification of a part with a complex shape. We clearly showed that the thickness shrinkage with different heights engender densification inhomogeneities.

Keywords:
Spark plasma sintering
Creep
Sintering parameters
Finite element method
Complex shape

1. Introduction

The modeling of the sintering process is extremely useful in that it allows the shrinkage of the sample and the final state of densification of a material (such as ceramics, metals or polymers) to be predicted. During sintering a wide range of mechanisms occur depending on the conditions and the process (e.g. free sintering, hot pressing, field assisted sintering) [1–3]. Natural sintering models [4] are based on the surface energy of the grains responsible for their coalescence and consequently for the densification of the powder. With Spark Plasma Sintering (SPS), a DC pulse current is used to raise the temperature of the column (tools + spacers) and simultaneously a uni-axial pressure is applied on the powder bed. To model sintering with applied pressure, models of porous solids built on creep law have been considered [5–7] – one of them is the Norton–Green model. For a given material, four main parameters need to be identified to use the complete Norton–Green model. Two of them are the Norton creep law parameters determined by creep experiments on dense materials at different temperatures and the two others: the Green functions c and f which are dependent on the relative density. Function f is usually determined by Hot Isostatic Pressing (HIP) of a porous material and function c can be determined by Hot-Pressing (HP) of a porous sample. Abouaf et al. [8–11] used this type of model to predict the sintering of a nickel super-alloy by HIP. Lately, Besson et al. [12,13] used the same approach to model the HIP sintering of alumina and also considered grain growth phenomena. Recently, Mondalek et al. [14,15] performed inverse analysis to determine Green's function parameters to describe the sintering of TiAl alloy by SPS. They also included in their model the friction between the powder and the parts of the mold. In the same way, Wolff et al. [16,17] determined Green's functions for a nickel powder based on the work of Nicolle [18] and an experimental identification.

Currently, one the most advanced theoretical work on modeling of sintering by SPS process is that of Olevsky and Froyen [19]. Their model contains three sintering phenomena, grain surface energy, electro-migration and the load effect. The classical version of Olevsky's model is closer to the Norton–Green model. For example, with alumina powder [1,20] this model only considers the creep

* Corresponding author. CIRIMAT, 118 route de Narbonne, 31062 Toulouse, France.
E-mail address: estournes@chimie.ups-tlse.fr (C. Estournès).

law (the load phenomenon) and the free sintering components. In the complete SPS model of Olevsky the coupling of the electro-thermal model and the sintering model has been considered. The load part of the model [1–3] contains like the Norton–Green model, some creep law parameters and two parameters depending on the porosity which have been theoretically determined for spherical pores [1,21].

In the present paper, we studied the sintering of a submicronic alumina powder and modeled its behavior using Olevsky's model. Different experiments in various conditions of heating rate and pressure have been made in order to determine their influence on the creep power laws parameters. Finally, a complex shape is generated and the FEM model is used to explain the relative density and microstructure heterogeneities observed in the real part.

2. Experimental

All the experiments were performed on the SPS machine (Dr. Sinter 2080, SPS Syntex Inc, Japan) of the Plateforme Nationale CNRS de Frittage Flash located at the Université Toulouse III-Paul Sabatier in Toulouse. For the determination of the creep law parameters, cylindrical molds (8 mm inner diameter – Fig. 1a) were used and each time 1 g of powder (alumina 99.99%, reference TM-DAR, Taimei Chemicals Co. Ltd) was loaded inside to ensure a shrinkage curve with enough amplitude to minimize error. The temperature set-point thermocouple was placed on the outer side of the die wall (3 mm in depth). To avoid any mistakes in identifying the sintering parameters all the experiments were performed in duplicate to obtain the real temperature of the sample. A second thermocouple was used, its extremity being located in the powder bed. The stress was evaluated by a load sensor and the strain by a displacement sensor located on the bottom electrode. The shrinkage of the powder compact was obtained by the column displacement minus the thermal expansion of the graphite determined with experiments on samples fully beforehand densified. For the study of the complex shaped part we used the configuration of classical uniaxial compaction (Fig. 1b).

Field-emission-gun scanning electron microscopy (FEG-SEM, JEOL JSM 6700F) observations on fractured samples were performed at the Temscan facility, Université Toulouse III Paul-Sabatier.

3. Theory

3.1. Model description

Olevsky's model is based on a creep power law defined for a porous viscous material.

$$\sigma(W) = KW^m \tag{1}$$

Where W is the equivalent strain rate, σ(W) the equivalent stress and K is the consistency factor. Other authors use another form of the creep law with the factor A and the n exponent instead of K and m. The following equations (2) and (3) are the temperature dependence of K and the conversion of the two forms of the creep law with K or with A.

$$K = \frac{1}{A_n^{\frac{1}{n}}} = \frac{1}{A_0^{\frac{1}{n}}} T^m \exp\left(\frac{mQ}{RT}\right) \tag{2}$$

$$m = \frac{1}{n} \tag{3}$$

where A, A_0 are the power law creep factors, T the absolute temperature, R the gas constant, Q the power law creep activation energy and n & m the exponents which are constants.

The power law creep equivalent strain rate of porous solids needs to define two functions of the porosity, the normalized shear modulus φ and the normalized bulk modulus ψ.

$$\varphi = (1-\theta)^2 \tag{4}$$

$$\psi = \frac{2}{3}\frac{(1-\theta)^3}{\theta} \tag{5}$$

The shrinkage rate $\dot{\gamma}$ and shape rate change $\dot{e}$ are functions of the strain rate tensor $\underline{\dot{\varepsilon}}$ components:

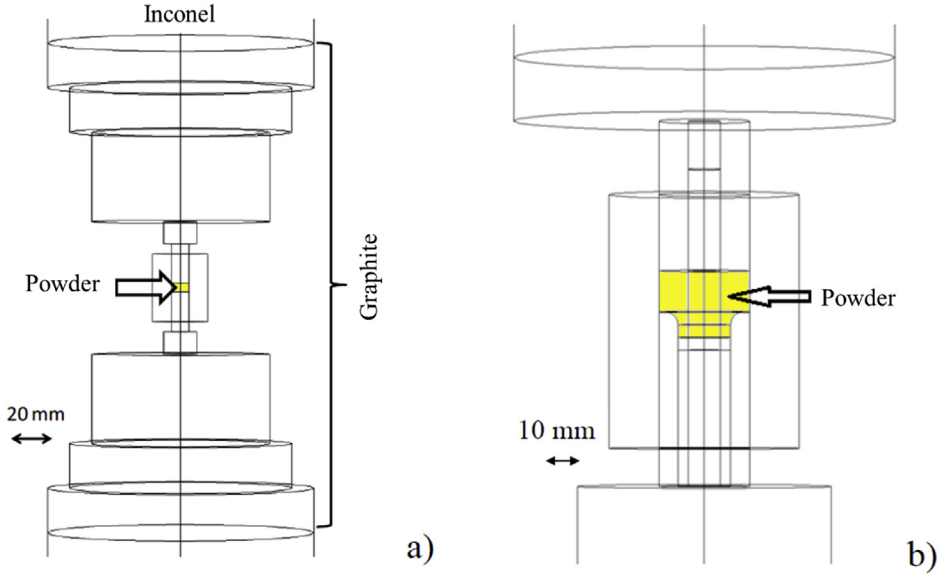

Fig. 1. a) SPS configuration used for the compression tests b) Complex shape part configuration.

$$\dot{\gamma} = \sqrt{2\left(\dot{\varepsilon}_{xy}^2 + \dot{\varepsilon}_{xz}^2 + \dot{\varepsilon}_{yz}^2\right) + \frac{2}{3}\left(\dot{\varepsilon}_x^2 + \dot{\varepsilon}_y^2 + \dot{\varepsilon}_z^2\right) - \frac{2}{3}\left(\dot{\varepsilon}_x\dot{\varepsilon}_y + \dot{\varepsilon}_x\dot{\varepsilon}_z + \dot{\varepsilon}_y\dot{\varepsilon}_z\right)} \tag{6}$$

with $\dot{e}$ the trace of the strain rate tensor $\underline{\dot{\varepsilon}}$.

The W expression of a porous material is defined as follows:

$$W = \frac{1}{\sqrt{1-\theta}}\sqrt{\varphi\dot{\gamma}^2 + \psi\dot{e}^2} \tag{7}$$

The stress tensor $\underline{\sigma}$ is expressed as:

$$\underline{\sigma} = \frac{\sigma(W)}{W}\left(\varphi\underline{\dot{\varepsilon}} + \left(\psi - \frac{1}{3}\varphi\right)\dot{e}i\right) + P_l i \tag{8}$$

where i is the identity tensor, Pl is the effective sintering stress of free sintering which is defined by:

$$P_l = \frac{3\alpha}{G}(1-\theta)^2 \tag{9}$$

where α is the surface energy and G the average grain diameter.

In our case P_l can be ignored because the rapid thermal kinetics combined with a high applied pressure make the creep part predominant.

The porosity θ is determined locally by the following mass conservation equation.

$$\frac{\dot{\theta}}{1-\theta} = \dot{\varepsilon}_x + \dot{\varepsilon}_y + \dot{\varepsilon}_z \tag{10}$$

3.2. Analytical equations for SPS

The case of SPS can be assimilated to uniaxial powder compaction (along the z-axis) in a die. Therefore, the external strain rate tensor can be reduced to:

$$\underline{\dot{\varepsilon}} \equiv \begin{pmatrix} 0 & 0 & 0 \\ 0 & 0 & 0 \\ 0 & 0 & \dot{\varepsilon}_z \end{pmatrix} \tag{11}$$

With (2, 7, 8) and (11), the stress z component expression becomes:

$$\sigma_z = KW^{m-1}\left(\varphi\dot{\varepsilon}_z + \left(\psi - \frac{1}{3}\varphi\right)\dot{\varepsilon}_z\right) \tag{12}$$

The shrinkage rate $\dot{\gamma}$ (6), shape rate change $\dot{e}$ and equivalent strain rate W (7) can be simplified in this way:

$$\dot{e} = \dot{\varepsilon}_z \tag{13}$$

$$\dot{\gamma} = |\dot{\varepsilon}_z|\sqrt{\frac{2}{3}} \tag{14}$$

$$W = |\dot{\varepsilon}_z|\sqrt{\frac{\psi + \frac{2}{3}\varphi}{1-\theta}} \tag{15}$$

3.3. Method of experimental identification of creep parameters by linear regression

As shown in Fig. 2, the sintering of the alumina powder is very fast, consequently the sintering usually occurs during the temperature ramp. It is thus better to determine an expression able to identify the creep parameters directly in the temperature ramp. Thus, in the following section we describe the constant heating rate identification method developed by Wang and Raj [22] and applied to the Olevsky model for the determination of the creep parameters.

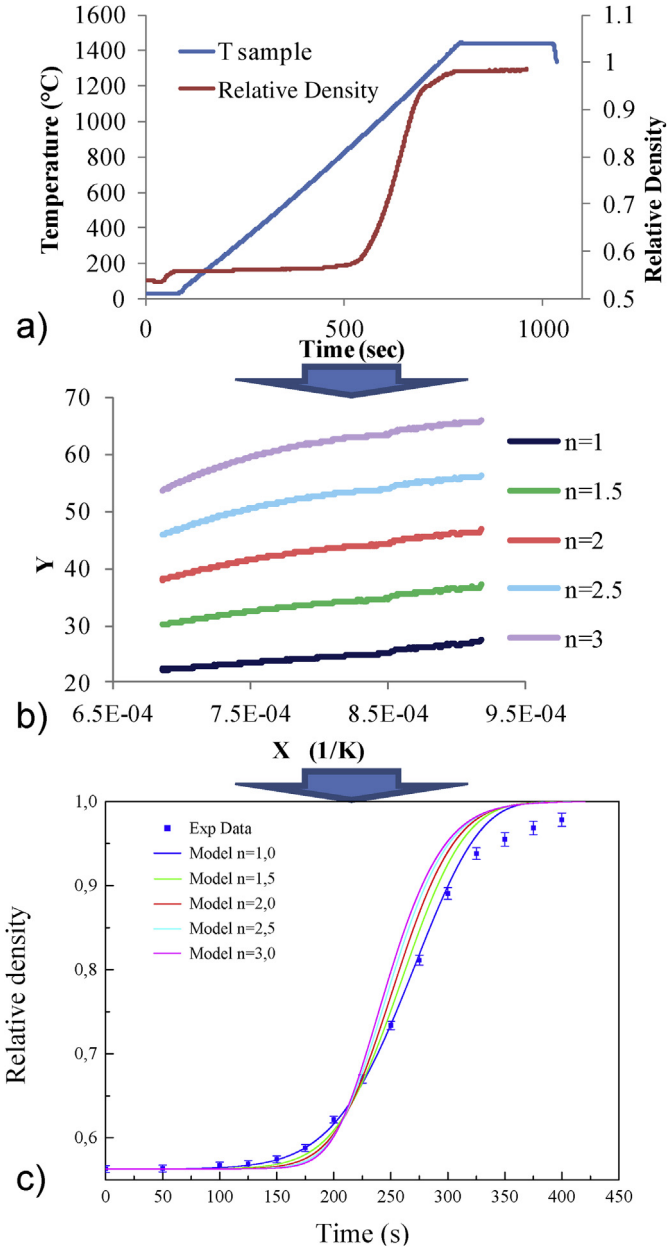

Fig. 2. Power law creep determination method (Taimei alumina, 100 K/min; 75 MPa): a) Experimental sintering cycle (Temperature and Relative Density). b) Linearization curves: Y vs 1/T. c) Modeled relative density for each tested n values (zoom in the densification area).

In order to determine the linearization equation at constant heating rate, we combine equations (2), (12) and (15) to obtain the strain rate z component in die compaction.

$$|\dot{\varepsilon}_z|^{\frac{1}{n}} = \frac{-A^{\frac{1}{n}}\sigma_z}{\left(\psi + \frac{2}{3}\varphi\right)^{1+\frac{1-n}{2n}}(1-\theta)^{\frac{n-1}{2n}}} \tag{16}$$

with in compression $\dot{\varepsilon}_z \leq 0$ consequently $\dot{\varepsilon}_z = -|\dot{\varepsilon}_z|$.

Table 1
All values of the constant A_0 and the activation energy Q at different heating rates and pressures for the strain exponent n = 1.

Temperature rate (K/min)	P (MPa)	A_0 (1/s)	Q (kJ/mol)	n
25	100	2.28E-01	192	1
50	100	3.55E-01	190	1
100	100	9.20E-01	195	1
200	100	1.60E-01	156	1
100	75	8.73E-01	179	1
75	75	2.47E-01	178	1
25	75	4.93E-02	161	1
25	125	2.26E-02	154	1
75	125	3.33E-02	158	1
100	125	1.95E-01	181	1

We introduce here the temperature dependence (17) of the power law creep factor A which is used by many authors [10,17,19] in an-isothermic regime. The Arrhenius form comes from the expression of the atomic diffusivity [3].

$$A = \frac{A_0 exp\left(\frac{-Q}{RT}\right)}{T} \tag{17}$$

Finally, combining equations (16) and (17) we obtain the linearization equation (18) used to determine the pre-exponential constant A_0 and the activation energy Q.

$$nln\left(\frac{|\sigma_z|}{\left(\psi+\frac{2}{3}\varphi\right)^{1+\frac{1-n}{2n}}(1-\theta)^{\frac{n-1}{2n}}|\dot{\varepsilon}_z|^{\frac{1}{n}}}\right) - \ln(T) = -ln(A_0) + \frac{Q}{RT} \tag{18}$$

with in compression $\sigma_z \leq 0$ and consequently $\sigma_z = -|\sigma_z|$.

All the left member terms are known by SPS experimental measures except constant n. Equation (18) can be identified with the linear function (19).

$$Y = a + bx \tag{19}$$

Where Y is the left member of equation (18) and x = 1/T.

A_0 is obtained by:

$$A_0 = exp(-a) \tag{20}$$

Q is obtained by:

$$Q = bR \tag{21}$$

The last parameter, the stress exponent n is determined by means of a comparative study. This methodology uses the high sensitivity of densification to this parameter. Indeed a non-suitable n value will not give a perfect fit of the experimental data points. Thus, we used linear regression to determine a set of couples (A_0; Q) for each n value. Next, each of these pairs of values are introduced into an analytical SPS model to find which one is the true value of n. The analytical model, executed on Octave software, uses equations (16) and (17) and the mass conservation equation (10).

4. Results and discussion

Paragraphs 4.1 and 4.2 are devoted to the determination of the creep power law parameters using the detailed linearization method for the experiments presented respectively in Fig. 2, obtained with various heating rate and pressure conditions. Paragraphs 4.3 and 4.4 are devoted to the study of the influence of the grain growth on the densification and the microstructure for both configurations and to the validation of the power law parameters determined in section 4.1.

4.1. Identification of the creep parameters

First the experimental data (relative density Fig. 2a, external strain rate and pressure) are taken into consideration to plot (Fig. 2b) the Y member of equation (18) as a function of the inverse of the temperature (1/T) for n ranging between 1 and 3 reasonable values for alumina considering the literature [22,23]. Moreover the

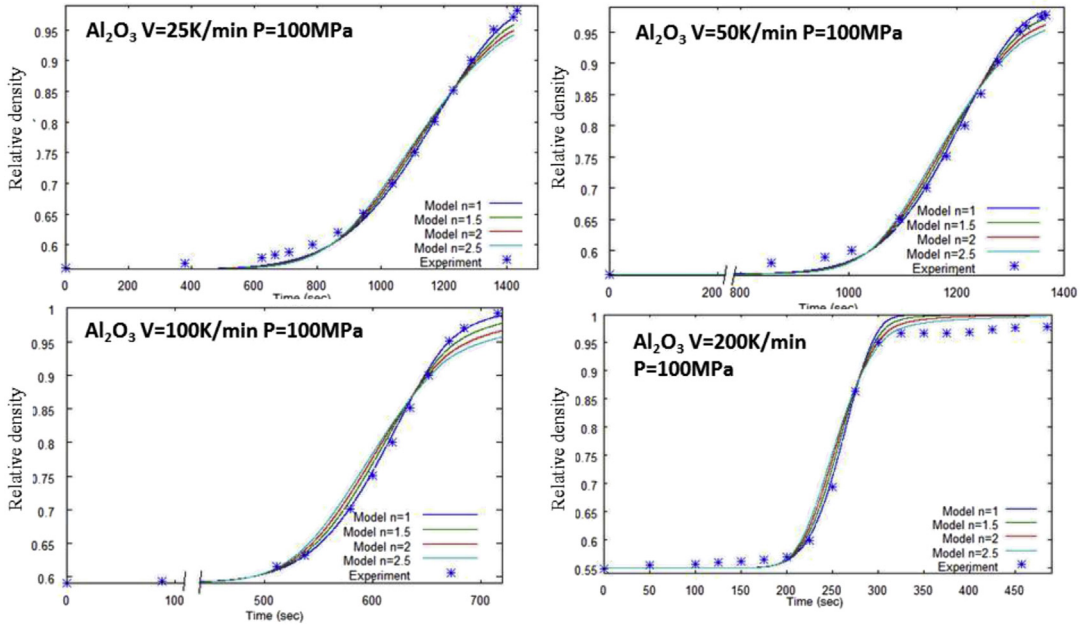

Fig. 3. Modeled relative density for different tested n, for various heating rate V (K/min) and a pressure of 100 MPa.

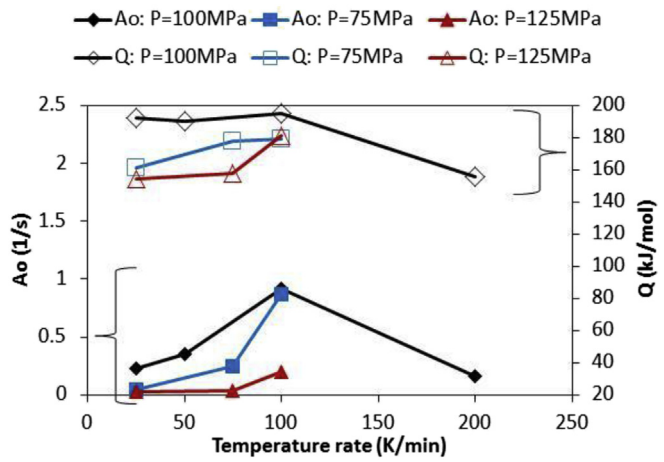

Fig. 4. Power law creep coefficients: A_0 and Q vs heating rate.

range of relative density of the analysis is limited to 0.9 because the effect of grain growth is drastically increased after this well-known threshold [24] and this will be discussed later.

Fig. 2b shows the best accordance of the regression for n close to 1. The next step is to determine the couple (A_0, Q) for each value of n and introduce this value into the analytical model. Fig. 2c reports the comparison of each modeled curve of the variation of relative density with temperature and the experimental points. Once again increasing the value of n increases the discrepancy between the experimental points and the calculated curves. This confirms that up to relative densities of 0.9, the value of n = 1 is in accordance with experiment. Above a relative density of 0.9 all calculated curves start to diverge probably due to an effect of grain growth (see section 4.3).

4.2. Power law creep parameters identification in various experimental conditions

In order to determine the effects of the heating rate and pressure on the power law creep parameters we used the set of experiments reported in Table 1. (see Fig. 3 and Appendix A) gathers the results of the nine experiments and shows the comparisons Model/Experimental using the linearization method developed in section 4.1. For all curves the best fit is obtained for n value equal to the unity (n = 1). Considering this latter in the model, the evolution of the identified values of A_0 and Q as a function of the heating rate (Fig. 4), shows a tendency of increase of A_0 and Q between 25 and 100 K/min and then a decrease for higher 200 K/min. The A_0 and Q parameters increase between 75 and 100 MPa and seems to decrease between 100 and 125 MPa, there is no obvious effect on the pressure. For each applied pressure, it is possible to write the power law creep expression depending of the heating rate in a

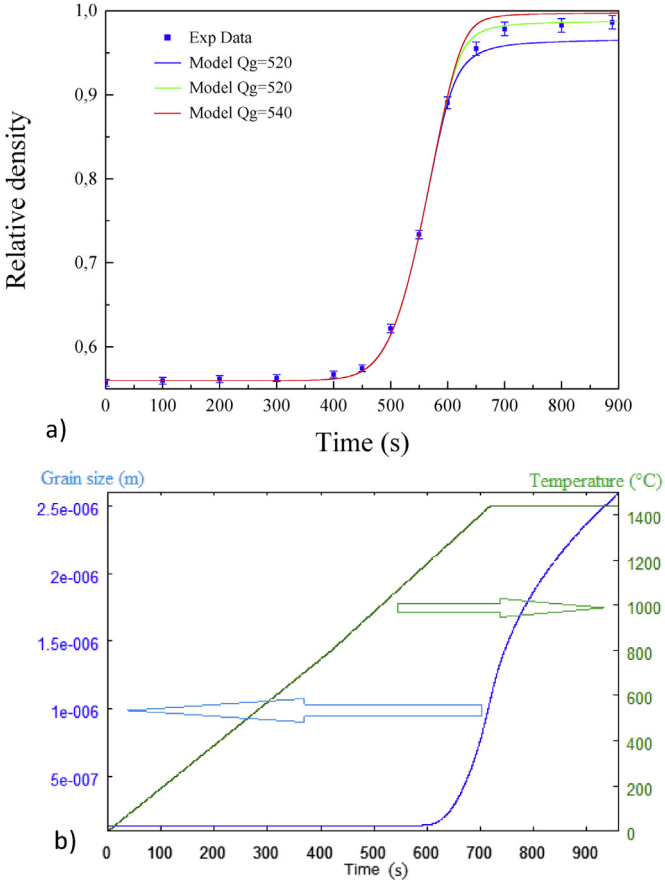

Fig. 5. a) Relative density curves in various grain activation energies Q_G. b) Grain size variation for Q_G = 520 kJ/mol.

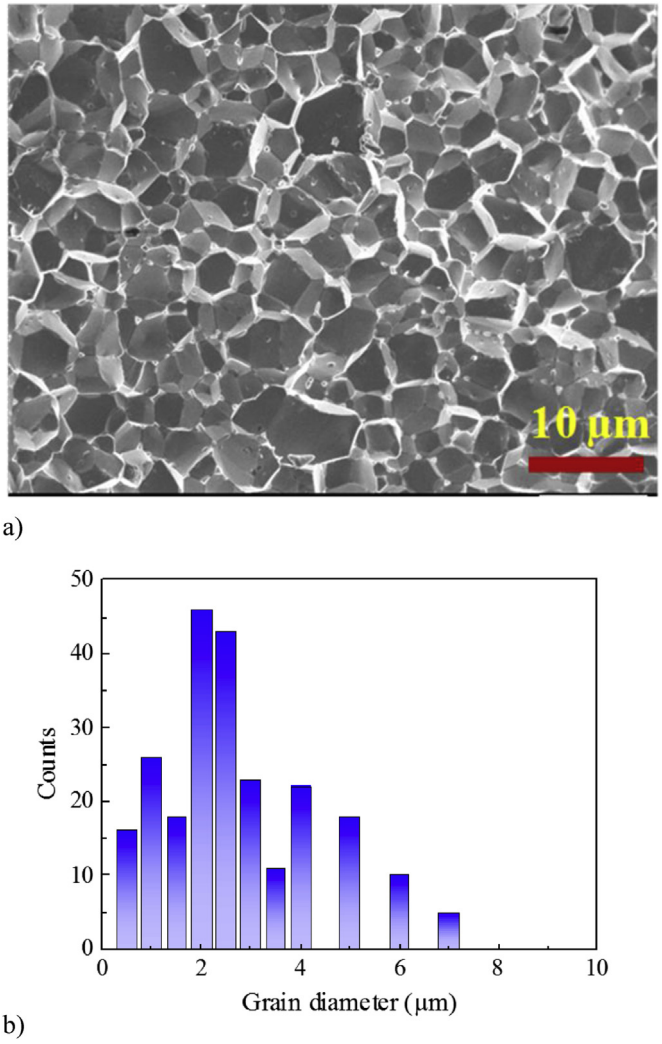

Fig. 6. a) Experimental grain size (SEM image of the final microstructure). b) Histogram of the grain size distribution.

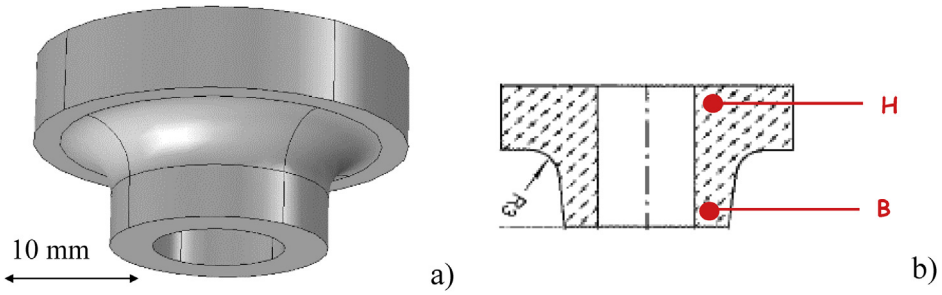

Fig. 7. a) Desired geometry, b) Cut plane with two strategic areas.

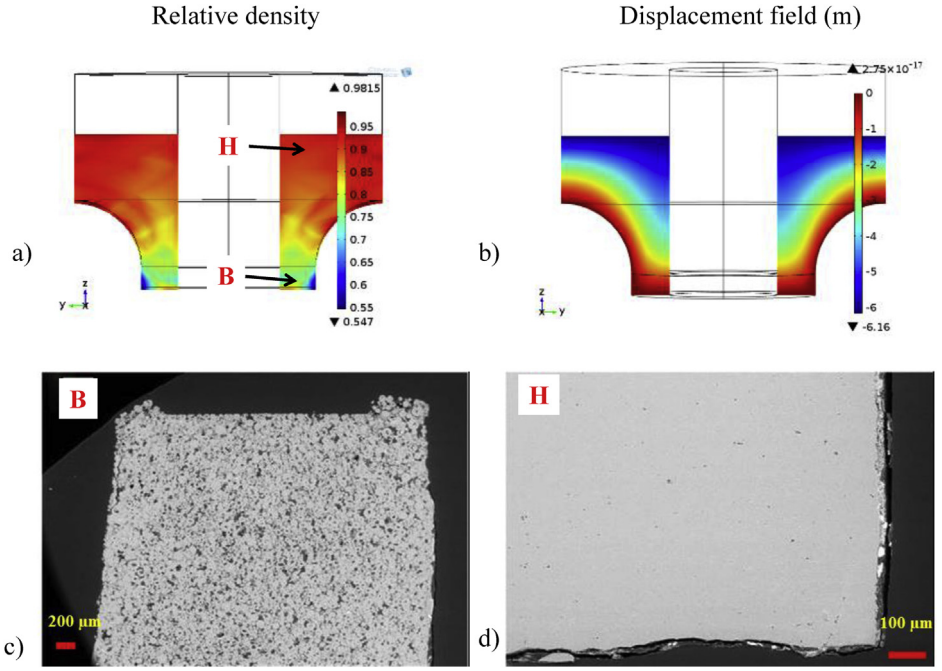

Fig. 8. Final stage of sintering in classical configuration: a) relative density. b) displacement on z. c) SEM image at point B. d) SEM image at point H.

domain ranging from 25 to 100 K/min (see Appendix A).

4.3. The grain growth effect

In the work of Gurt-Santanach et al. [24] performed on the same submicronic α-alumina powder, grain growth was observed to start above a temperature of 1000 °C. The experiment reported in Fig. 2 has a dwell temperature of 1200 °C and the relative density curve at the end of the cycle seems to slow down and looks like an asymptotic curve with a final relative density of 0.987. In contrast, Fig. 2c shows at the end of a cycle an asymptotic variation of the density close to full relative density (relative density = 1) instead of 0.987. The discrepancy between the calculated and experimental values may be attributed to a grain growth phenomenon which is known to slow down the densification rate [4]. The grain growth law is known to be thermally activated [24]. According to Olevsky's model [3] for alumina, the granular growth law defined by equation (22) also depends on the porosity (θ).

$$\dot{G} = \frac{k_0}{3G^2}\left(\frac{\theta_c}{\theta_c+\theta}\right)^{\frac{3}{2}} exp\left(\frac{-Q_G}{RT}\right) \tag{22}$$

Then, the creep law is affected by the grain size as in equation (23)

$$K = \left(\frac{G}{G_0}\right)^2 \frac{1}{A_0^{\frac{1}{n}}} T^m \exp\left(\frac{mQ}{RT}\right) \tag{23}$$

where G is the average grain diameter, G_0 the initial grain diameter of 0.14×10^{-6} m, k_0 a constant of 7×10^{-4} m^3/s, Q_G is the activation energy of the grain growth and θ_c a critical porosity of 0.05.

An increase of the grain size during the cycle (i.e. the ratio G/G_0) leads to an increase in K and thus to a corresponding decrease of the sintering rate. The calculated relative density curves with different values of the grain growth activation energy (Q_G) (Fig. 5a), confirm the strong influence of this phenomenon on the final stages of sintering. A high value of Q_G implies limited grain growth that leads, at the final stage, to a relative density curve approaching a value of 1. By contrast, a low value of Q_G leads to strong grain growth that slows the sintering rate, the calculated relative density curve at the final stage of sintering remaining below the experimental relative density points. A good agreement of the final behavior of the calculated relative density with the experimental points was obtained with a value of the activation energy of Q_G = 520 kJ/mol. Introducing this value into equation (22), the average grain size was calculated to be 2.6 µm (Fig. 5a). The SEM image (Fig. 6a) of a fractured surface of the sample indicates the

experimental distribution of the grain size (Fig. 6b) and gives an average value of 2.7 μm ± 1.5 μm. The final grain size given by the model seems to be in very good agreement with experiment.

4.4. Finite element approach

The mechanical approach previously described was then coupled, by finite element method (FEM) configuration in a COMSOL Multiphysics code (version 4.3b) with the already described electro-thermal model [25] and adapted to the present study for the densification of a complex shaped part (Fig. 7). The densification in classical uniaxial configuration detailed in Fig. 1b is modeled and the results are reported in Fig. 8. It is to be noted that the thickness differences of the complex shape imply strong relative density gradients in the sintered part. The bottom zones of the areas of initial high thickness (Fig. 7b point B) remain porous while the others (Fig. 7b point H) are nearly fully densified (Fig. 8a). In these zones, the material need more shrinkage (in the compression direction) to be fully densified compared to the thinner ones. These latter are thus first densified and then block the stroke of the punches. Thus, the displacement field appears with bent curves (Fig. 8b). In accordance with the simulation, SEM images reveal high level of porosity (20% by image analysis) at point B (Fig. 8c) and a nearly fully dense microstructure at point H (Fig. 8d). The strategies implemented to resolve these heterogeneities and gradients will be presented in an other publication.

5. Conclusion

The first part of this work presents a methodology for the determination of the creep parameters using Olevsk's model. The method consists of three main parts:

- First, a linear regression of the experimental data up to relative densities around 0.9 is performed to determine the power law creep parameters: the pre-exponential factor (A_0) and the activation energy (Q) for different values of the strain exponent n.
- The analytic model compares the different couples (A_0, Q) and locates the suitable n value.
- The parameters corresponding to grain growth can be determined with the final part of the experimental relative density curve.

This empiric methodology can be used to determine the sintering parameters of a material with simple SPS experiments. The main advantage of this method is its ability to rapidly obtain sintering parameters of a material with few SPS experiments compared to classical studies that use a lot of mechanical tests involving lengthy experiments and characterizations.

The modeling of uniaxial compaction of a complex shape shows very good agreement between experiment and simulation and highlights the problem of height shrinkage differences that creates areas of high porosity gradients.

Acknowledgments

The support of the Plateforme Nationale CNRS de Frittage Flash (PNF2/CNRS) is gratefully appreciated. C.M and C.E. thank the French National Research Agency (ANR) ANR009 MAPR-007 for financial support of this study within project ANR09 MAPR-007 Impulsé.

Appendix A. Supplementary data

Supplementary data related to this article can be found at http://dx.doi.org/10.1016/j.actamat.2015.09.003.

References

[1] E.A. Olevsky, Theory of sintering: from discrete to continuum, Mater. Sci. Eng. R. 23 (1998) 41–100.
[2] E.A. Olevsky, W.L. Bradbury, C.D. Haines, D.G. Martin, D. Kapoor, Fundamental aspects of spark plasma sintering: I. Experimental analysis of scalability, J. Am. Ceram. Soc. 95 (2012) 2406–2413.
[3] E.A. Olevsky, C. Garcia-Cardona, W.L. Bradbury, C.D. Haines, D.G. Martin, D. Kapoor, Fundamental aspects of spark plasma sintering: II. Finite element analysis of scalability, J. Am. Ceram. Soc. 95 (2012) 2414–2422.
[4] M.N. Rahaman, Sintering of Ceramics, CRC Press, 2008.
[5] A.S. Helle, K.E. Easterling, M.F. Ashby, Hot-isostatic pressing diagrams: New developments, Acta Metall. 33 (1985) 2163–2174.
[6] G. Bernard-Granger, C. Guizard, Spark plasma sintering of a commercially available granulated zirconia powder: I. Sintering path and hypotheses about the mechanism(s) controlling densification, Acta Mater. 55 (2007) 3493–3504.
[7] J. Langer, M.J. Hoffmann, O. Guillon, Direct comparison between hot pressing and electric field-assisted sintering of submicron alumina, Acta Mater. 57 (2009) 5454–5465.
[8] R.J. Green, A plasticity theory for porous solids, Int. J. Mech. Sci. 14 (1972) 215–224.
[9] M. Abouaf, Modelisation de la compaction de poudres métalliques frittées. Approche par la mécanique des milieux continus (PhD thesis), Institut national polytechnique de Grenoble, 1985.
[10] M. Abouaf, J.L. Chenot, Modelisation numérique de la déformation à chaud de poudres métalliques, JTAM 5 (1986) 121–140.
[11] M. Abouaf, J.L. Chenot, G. Raisson, P. Bauduin, Finite element simulation of hot isostatic pressing of metal powders, Int. J. Numer. Methods Eng. 25 (1988) 191–212.
[12] J. Besson, Simulation numérique de la mise en forme des céramiques application à la compaction isostatique à chaud (PhD thesis), Ecole nationale supérieure des mines de Paris, 1990.
[13] J. Besson, M. Abouaf, Numerical simulation of hot isostatic pressing of ceramic powders, Proc. Int. Conf. Hot Isostatic Press. Mater. 25 (1988), 1.17-1.22.
[14] P. Mondalek, Numerical modeling of the spark plasma sintering process Ecole nationale supérieure des mines de Paris (PhD thesis), 2012.
[15] P. Mondalek, L. Silva, M. Bellet, Modélisation numérique électrique-thermique-mécanique du procédé de frittage flash, Conf. Mater. 2010 (2010).
[16] C. Wolff, Modélisation du processus thermo-électro-mécanique de Frittage Flash (PhD thesis), University Paul Verlaine of Metz, 2011.
[17] C. Wolff, S. Mercier, H. Couque, A. Molinari, Modeling of conventional models of porous materials, Mech. Mater. 49 (2012) 72–91.
[18] C. Nicolle, Mise en forme de poudres de bore par compression isostatique à chaud: Détermination des proprieties rhéologiques et simulation numérique du procédé (PhD thesis), Bourgogne University, 1999.
[19] E.A. Olevsky, L. Froyen, Impact of thermal diffusion on densification during SPS, J. Am. Ceram. Soc. 92 (2009) S122–S132.
[20] V.V. Skorokhod, E.A. Olevsky, M.B. Shtern, Continuum theory of sintering. I. Phenomenological model. Analysis of the effect of external forces on the kinetics of sintering, Powder Metall. Met. Ceram. 93 (1933) 1068–1302.
[21] V.V. Skorokhod, Rheological Basis of the Theory of Sintering, Naukova Dumka, Kiev, 1972.
[22] L.A. Xue, I.W. Chen, Deformation and grain growth of low-temperature-sintered High-purity Alumina, J. Am. Ceram. Soc. 73 (1990) 3518–3521.
[23] O. Flacher, J.J. Blandin, K.P. Plucknett, Effects of zirconia additions on the superplasticity of alumina-zirconia composites, Mater. Sci. Eng. A 221 (1996) 102–112.
[24] J. Gurt Santanach, A. Weibel, C. Estournès, Q. Yang, Ch Laurent, A. Peigney, Spark plasma sintering of alumina: study of parameters, formal sintering analysis and hypotheses on the mechanism(s) involved in densification and grain growth, Acta Mater. 59 (2011) 1400–1408.
[25] A. Pavia, L. Durand, F. Ajustron, V. Bley, G. Chevallier, A. Peigney, et al., Electro-thermal measurements and finite element method simulations of a spark plasma sintering device, J. Mater. Process Tech. 213 (2013) 1327–1336.